NANO LETTERS

Letter

pubs.acs.org/NanoLett

# Selective Ionic Transport Pathways in Phosphorene

Anmin Nie,[†] Yingchun Cheng,[†,⊥] Shoucong Ning,[‡] Tara Foroozan,[§] Poya Yasaei,[†] Wen Li,[∥] Boao Song,[†] Yifei Yuan,[†] Lin Chen,[#] Amin Salehi-Khojin,[†] Farzad Mashayek,*[,†] and Reza Shahbazian-Yassar*[,†]

[†]Department of Mechanical and Industrial Engineering, University of Illinois at Chicago, Chicago, Illinois 60607, United States

[⊥]Key Laboratory of Flexible Electronics (KLOFE) & Institute of Advanced Materials (IAM), Jiangsu National Synergistic Innovation Center for Advanced Materials (SICAM), Nanjing Tech University, 30 South Puzhu Road, Nanjing 211816, China

[§]Department of Civil and Materials Engineering, University of Illinois at Chicago, Chicago, Illinois 60607, United States

[∥]Department of Biological and Chemical Sciences, Illinois Institute of Technology, Chicago, Illinois 60616, United States

[‡]Department of Mechanical and Aerospace Engineering, Hong Kong University of Science and Technology, Clearwater Bay, Kowloon, Hong Kong SAR, P. R. China

[#]Energy Systems Division, Argonne National Laboratory, Lemont, Illinois 60439, United States

Supporting Information

**ABSTRACT:** Despite many theoretical predictions indicating exceptionally low energy barriers of ionic transport in phosphorene, the ionic transport pathways in this two-dimensional (2D) material has not been experimentally demonstrated. Here, using in situ aberration-corrected transmission electron microscopy (TEM) and density functional theory, we studied sodium ion transport in phosphorene. Our high-resolution TEM imaging complemented by electron energy loss spectroscopy demonstrates a precise description of anisotropic sodium ions migration along the [100] direction in phosphorene. This work also provides new insight into the effect of surface and the edge sites on the transport properties of phosphorene. According to our observation, the sodium ion transport is preferred in zigzag edge rather than the armchair edge. The use of this highly selective ionic transport property may endow phosphorene with new functionalities for novel chemical device applications.

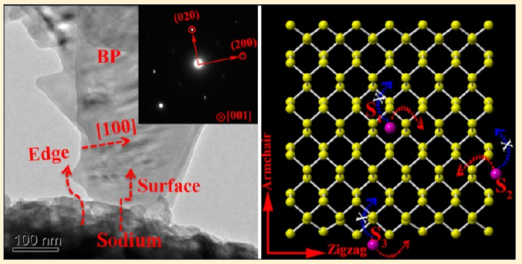


**KEYWORDS:** *Phosphorene, ionic transport, edge effect, rechargeable ion battery, in situ electron microscopy*

Solid conductors, exhibiting significant electronic and ionic conductivity, are very important components in electrochemical devices, chemical sensors, chemical reactors, chemical filters, and electrochromic windows.[1] Exploration of mixed electronically and ionically conducting solids is a key to promote the development of the next generation electrochemical devices. Accordingly, two-dimensional (2D) materials, from the first discovered graphene[2,3] up to the recently synthesized transition metal dichalcogenides[4,5] and MXene,[6,7] have been widely explored as mixed conductors for their potential applications in electrochemical devices due to their fast ionic conductivity and unique electronic properties. Among 2D materials, the monolayer black phosphorus (BP), phosphorene, with distinct in-plane anisotropic electrical, optical and phonon properties,[8−14] has presently captured the attention of scientific community for potential applications in many practical devices such as rechargeable ion batteries,[15−20] solar cells,[21−23] field-effect transistors,[8,24,25] thermoelectric,[26−28] sensors,[29] and optoelectronic[9,11,12] devices. The orthorhombic black phosphorus possesses a layered structure with a unique puckered honeycomb structure.[30,31] Sharing structural similarities with graphite by weak interlayer van de Waals (vdW) interactions, few-layer and monolayer phosphorene can be isolated by mechanical cleavage[25] and liquid phase exfoliation methods.[32] The studies of ionic transport in phosphorene holds great potential to impact emerging technologies such as electrochemical batteries, fuel cells, and chemical sensors. For instance, the rechargeable batteries field[33−39] is an important domain where phosphorene can find its potential application. Recently, successive theoretical studies[15−19] have been performed to investigate the binding and diffusion behavior of lithium (Li) and sodium (Na) in phosphorene. For example, density functional theory (DFT) calculations[19] have indicated that the diffusion of Li in phosphorene is highly anisotropic with an extremely low diffusion barrier (0.08 eV) along the zigzag direction, leading to an ultrahigh diffusivity $10^2$ ($10^4$) times faster than that of $MoS_2$[40] (graphene[41]) at room temperature. Additionally, the intercalation of Li triggers a semiconducting to metallic transition, leading to a good electrical conductivity in phosphorene. In addition, the first-principles calculations[17] have predicted a favorable Na−phosphorene interaction with a

**Received:** November 5, 2015
**Revised:** March 7, 2016
**Published:** March 17, 2016





DOI: 10.1021/acs.nanolett.5b04514
*Nano Lett.* 2016, 16, 2240−2247

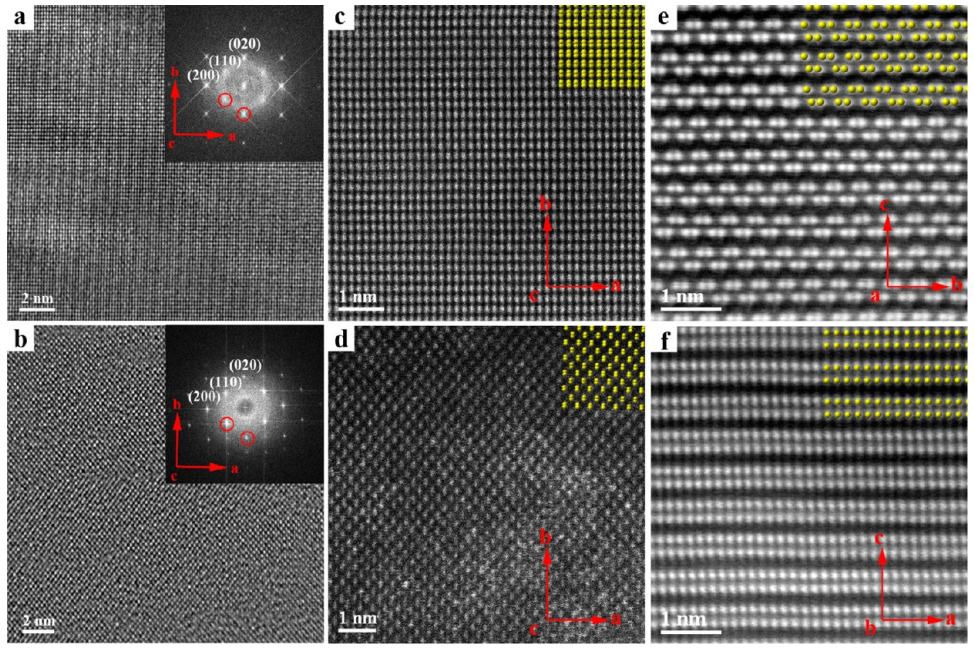


**Figure 1.** Atomic-scale TEM and STEM imaging of few-layer and monolayer phosphorene. (a, b) HRTEM images of few-layer and monolayer phosphorene viewed along the [001] direction, respectively. Insets of the panels show the corresponding fast Fourier transform (FFT) of HRTEM image. (c, d) Atomic-scale HAADF images of few-layer and monolayer phosphorene viewed along the [001] direction, respectively. Insets of the panels show corresponding atomic models. (e, f) Atomic-scale HAADF images of few-layer phosphorene viewed along the [100] and [010] directions, respectively. Insets of the panels show the corresponding atomic models.

high sodium storage (865 mA h $g^{-1}$ for double-side Na adsorption) ability and an ultrafast Na diffusivity in preferred directions. Theoretical predictions claim that the energy barrier for Na diffusion in phosphorene can be extremely low (0.04 eV), being smaller than that of graphene (0.10 eV),[42] sillicene (0.12 eV),[43] and monolayer $MoS_2$ (0.28 eV).[44] However, to date, there has been no direct experimental evidence of ionic transport pathways in phosphorene, which is important for understanding and exploring phosphorene based solid conductors.

In the following, we present an experimental study of sodium ion transport in few-layer and monolayer phosphorene by using state-of-the-art in situ transmission electron microscopy (TEM). Our atomic scale observation reveals a highly anisotropic diffusion pathway for sodium ions transport in phosphorene. We observed that sodium ions prefer to diffuse along the [100] direction in phosphorene. The DFT calculation was also used to explore the diffusivity of sodium ions in phosphorene and gain an insight into the effect of surface and the edge sites on the transport properties of phosphorene.

The few-layer and monolayer phosphorene used in this study were characterized by high-resolution TEM (HRTEM) and atomic scale high angle annular dark field (HAADF) imaging. Figure 1a shows a typical HRTEM image of few-layer phosphorene viewed with the [001] zone axis. The corresponding fast Fourier transform (FFT) pattern indicates the orientation of this atomically thin sheet, shown in the inset of Figure 1a. As theoretically indicated, the intensity ratio of the (110) to (200) diffraction peaks ($I_{110}/I_{200}$) is thickness dependent.[45] For Figure 1a, the $I_{110}/I_{200}$ is about 0.5 (Supplementary Figure S1), which is consistent with the ratio predicted for a few layer thick sample. The HRTEM image of monolayer phosphorene is distinguished from that of few-layer phosphorene by its hexagonal-like pattern as shown in Figure 1b (Supporting Information, Figures S3c and 4). The FFT pattern of Figure 1b shows strong {110} spots and the $I_{110}/I_{200}$ is as high as 2.5 (Supporting Information, Figure S1), in good agreement with the experimental value of 2.5−2.9 for monolayer phosphorene.[32] The selected area electron diffraction (SAED) patterns also indicate that the {110} spots are much stronger than the {020} spots for the monolayer sample (Supporting Information, Figure S2). The atomic scale HAADF image (Figure 1c) clearly shows the atomic arrangement of the few-layer phosphorene sample with an orthogonal pattern due to ABAB stacking sequence of the (001) phosphorus layers along the [001] direction. The well-known atomic structure of phosphorene projected in the *c* direction is overlapped on Figure 1c. Our experimental observation perfectly matches with this atomic model. The atomic structure of phosphorene is also resolved by atomic scale HAADF, as shown in Figure 1d. The atomic scale HAADF image more clearly presents the hexagonal-like atomic arrangement of monolayer phosphorene. To the best of the authors' knowledge, Figure 1d displays the first published atomic scale HAADF image of phosphorene. The atomic model of monolayer phosphorene is also inserted in Figure 1d verifying our experimental observation. The atomic scale HAADF images of few-layer phosphorene in the [100] and [010] directions are also supported in Figure 1e and f. We can clearly see the puckered atomic structure of the few-layer phosphorene by viewing in the [100] direction. The simulation of STEM and HRTEM images of few-layer and monolayer phosphorene has also been performed as shown in Figure S4 (Supporting Information).

Movie S1 and S2 (Supporting Information) show the sodiation process of individual few-layer thick phosphorene flakes. Interestingly, many gray-contrast stripes with specific orientation in the few-layer phosphorene after applying negative bias on nanoflake. The schematic of the experimental setups can be found at the inset of Figure 2. The formation of the stripes was also clearly demonstrated by the in situ TEM



DOI: 10.1021/acs.nanolett.5b04514
*Nano Lett.* 2016, 16, 2240−2247

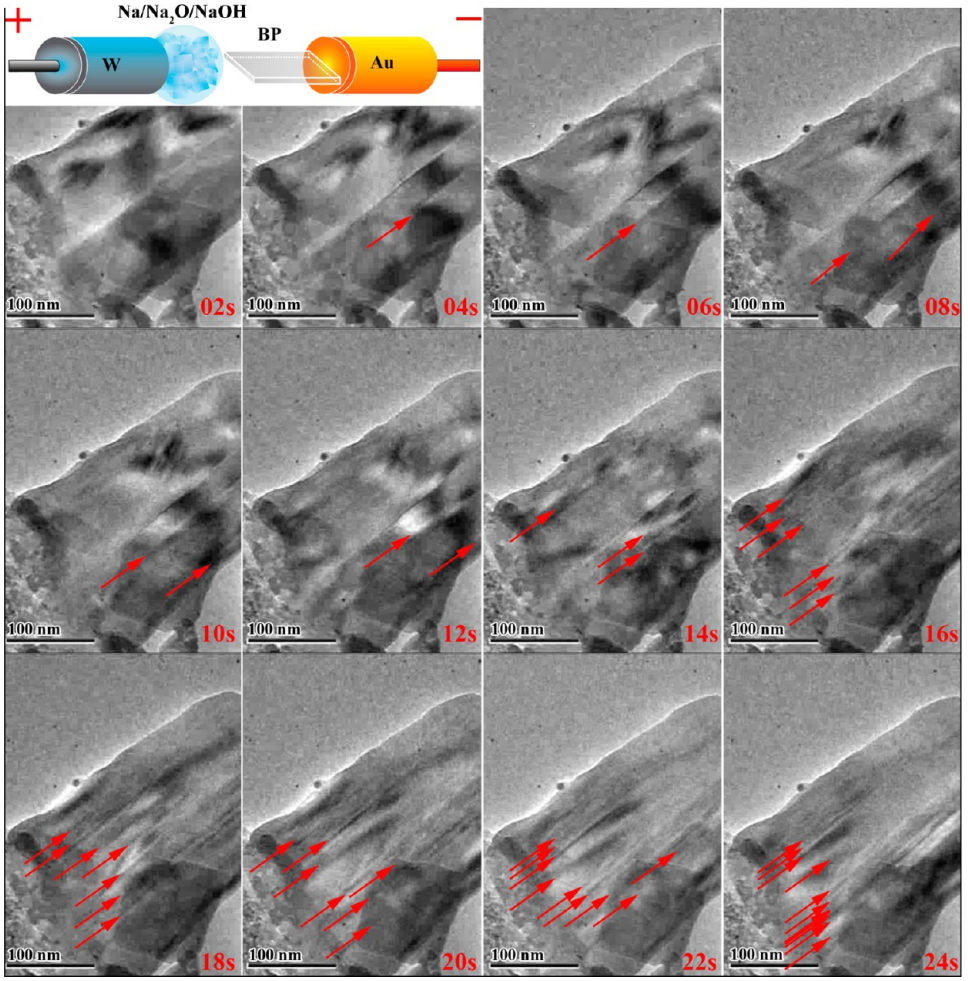


**Figure 2.** In situ TEM snapshots showing the structure evolution of a few-layer phosphorene nanoflake during the sodium transport process. Images are taken during the first 24 s of sodium ion transport process. The red arrows indicate the position of the formed stripes. The inset is the schematic of the experimental setups.

snapshots in Figure 2. The red arrows indicate the dynamic evolution of stripes during the sodiation of the few-layer phosphorene. Figure S5 (Supporting Information) shows typical static TEM images of partially sodiated few-layer phosphorene. We can clearly see the sodiation stripes across the few-layer phosphorene flakes. Figure 3a displays a HRTEM image of partially sodiated few-layer phosphorene taken with the [001] zone axis. According to the orientation analysis of Figure 3a, the sodiation stripes are along the [100] direction parallel to the (020) lattice plane of few-layer phosphorene. The analysis indicates that the sodium ions prefer to diffuse along the [100] direction rather than taking place along the other directions inside few-layer phosphorene. The lattice near the stripes is distorted due to sodium intercalation (Figure S6). The existence of sodium element in the stripes has also been detected by electron energy loss spectroscopy (EELS) (Figure 3b). The sodiation process of monolayer phosphorene is also captured by in situ TEM. Figure 3c shows a HRTEM image of slightly sodiated monolayer phosphorene. The feature of the corresponding FFT pattern (inset of Figure 3c) is similar to that of Figure 1b. The sodiation trace (marked with the red arrow) with gray contrast can be distinguished from the perfect lattice area in Figure 3b. Similar to sodiation of few-layer phosphorene, the sodiation stripe in monolayer phosphorene is also along the [100] direction.

Interestingly, we have observed that the sodiation stripes along the [100] direction are always formed regardless of the contact geometry between the phosphorene nanoflake and sodium source (Supporting Information Movie S1, S2 and Figure 4). As illustrated in Figure 4a, the contact interface is normal to the [100] direction and the multiple sodiation stripes directly propagate from the sodium source toward the few-layer phosphorene sheet. Figure 4b shows another case where the contact interface is parallel to the [100] direction and the multiple sodiation stripes initiate from the edge side across the few-layer phosphorene nanoflake. Accordingly, it is puzzling why the sodium ions initially migrate into [100] diffusion channels if the channels in phosphorene do not directly touch the sodium source.

To better understand this selective diffusional behavior, sodium ion diffusion between the layers of phosphorene was further investigated by means of the DFT calculation. Figure 5a shows a schematic of sodium atom transport in the interlayer of few-layer phosphorene in the [100] (red arrow) and [010] (blue arrow) directions. The energy profiles for sodium diffusion inside atomically thin phosphorene along two diffusion directions are presented in Figure 5b. For the case of Na diffusion along the [010] direction (the blue curve in Figure 5b), the energy barrier is about 0.64 eV. However, for the diffusion along the [100] direction (the red curve), a rather



DOI: 10.1021/acs.nanolett.5b04514
Nano Lett. 2016, 16, 2240−2247

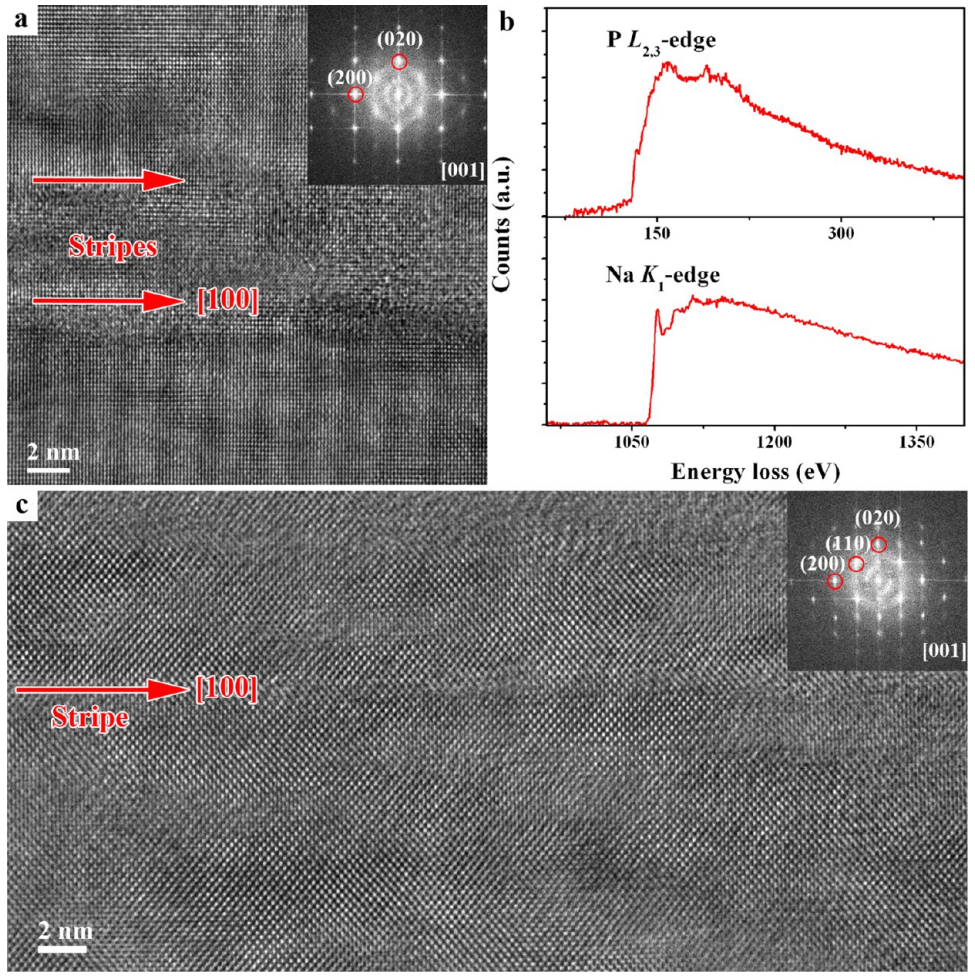


**Figure 3.** Sodium ion transport in few-layer and monolayer phosphorene. (a) HRTEM image of partially sodiated few-layer phosphorene viewed in the [001] direction. The inset shows corresponding FFT pattern. (b) EELS spectra collected at the stripe of partially sodiated monolayer phosphorene. The P $L_{2,3}$ edge (132 eV) and Na $K_1$ edge (1072 eV) are captured at the stripe. (c) HRTEM image of partially sodiated phosphorene with the top view. Inset shows corresponding FFT pattern.

smaller energy barrier of 0.08 eV is shown. Accordingly, the diffusion constant can be evaluated by the following equation:[19,41]

$$D \sim \exp(-E_a/k_B T)$$

where $T$ is the temperature (300 K at room temperature), $k_B$ is Boltzmann's constant ($8.617 \times 10^{-5}$ eV/K), and $E_a$ is the diffusion barrier obtained by the DFT calculation. According to this equation, the diffusion mobility of sodium in the [100] direction is about $2.8 \times 10^9$ faster than that along the [010] direction. This result well explains why the sodium-rich stripes are along the [100] direction.

In order to quantify the diffusion of sodium on the surface of monolayer phosphorene, DFT calculations have also been performed. Figure 5c shows schematic of sodium atoms transport with different pathways in phosphorene. The energy profiles for sodium diffusion on the surface ($S_1$) of monolayer phosphorene are summarized in Figure 5d. The energy barriers for sodium diffusion along the armchair and zigzag directions are 0.39 and 0.04 eV, respectively. Likewise, strong diffusion anisotropy is observed and sodium diffusion along the zigzag direction dominated in monolayer phosphorene. Compared to few-layer phosphorene, the sodium diffusion on phosphorene is associated with lower energy barriers. Therefore, it is expected that monolayer phosphorene-based sodium-ion batteries would exhibit a higher rate capability (4.7 times faster) than those based on few-layer phosphorene.

To address the question why the sodium ions initially migrate into [100] diffusion channels if the channels in phosphorene do not directly touch the sodium source, we performed DFT calculation to investigate the effect of edge and surface sites on the sodium ion transport in phosphorene. Figure 5e shows the energy profiles for sodium atom diffusing along the zigzag edge and the armchair surface ($S_2$). The energy barrier for sodium atom migration from the zigzag edge onto the surface is about 0.38 eV. By contrast, only 0.11 eV of energy is need for a sodium atom to migrate along the zigzag edge. This suggests that the sodium atoms on the zigzag edge tend to diffuse along the edge sites and not through the surface. The energy profiles of sodium diffusion along the armchair edge and zigzag surface (S3) are displayed in Figure 5f. As illustrated in Figure 4b, the energy decreases after migrating onto the zigzag surface. Comparatively, there is a 0.35 eV energy barrier for the sodium atom migration along the armchair edge. This means that the sodium atom on the armchair edge prefers to diffuse onto the surface instead of diffusing along the edge.

To gain better insight of transport pathways for other ions, lithium ion transport in phosphorene was also evaluated, and



DOI: 10.1021/acs.nanolett.5b04514
Nano Lett. 2016, 16, 2240−2247

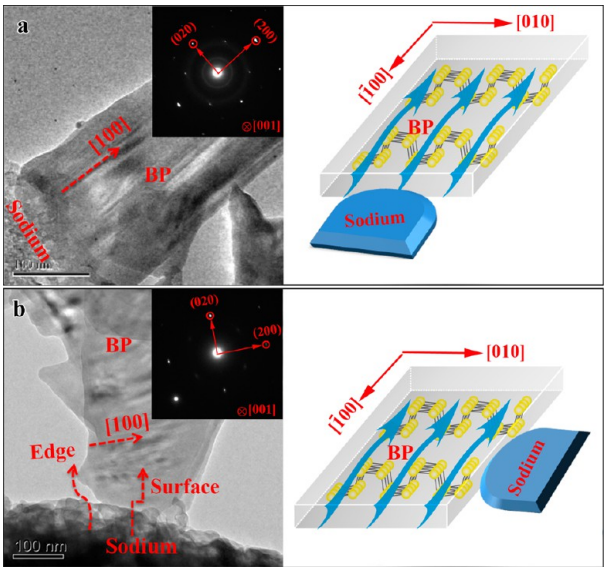


**Figure 4.** Sodium transport in few-layer phosphorene with different contact geometries with respect to the sodium source. (a) Contact interface normal to the [100] direction. The inset shows corresponding electron diffraction pattern of the few-layer phosphorene in panel a. (b) Contact interface parallel to the [100] direction. The inset shows the corresponding SAED pattern of the few-layer phosphorene in panel b.

the results are shown in Figure S7. Interestingly, the stripes were also observed during lithiation; however, the contrast of such stripes was much weaker than sodiated-induced ones. The lower contrast is expected to be due to smaller size of lithium ions in comparison to sodium ions resulting in less lattice distortion of the phosphorene. We believe that this anisotropic ionic diffusion in phosphorene can be applicable for different ions due to intrinsic nature of phosphorene.

It should also be noted that the above experimental observation was conducted at initial sodiation stage. A previous study has indicated that the storage of sodium ions in black phosphorus proceeds by a two step mechanism of intercalation and alloying.[20,46] Alloying reaction between the sodium and phosphorene has also been observed by our in situ sodiation experiments. As shown in Figure S8, the structure of the phosphorene finally changed into amorphous sodium phosphide after a full sodiation, which is highly consistent with the previous first-principle calculations.[46] Noticeably, the exfoliated phosphorene sample shows excellent cyclability during in situ sodiation/desodiation testing. Figure 6 and Movie S4 show a few-layer phosphorene specimen subjected to sodiation and desodiation for multiple times. In spite of observed severe volume change, the specimens cycled well without any detectable fracture.

The electrochemical performance of phosphorene for half-cell sodium-ion batteries has also been investigated. Figure 7a shows cyclic voltammetry (CV) of the first three cycles for the phosphorene sample at a scan rate of 0.05 mV $S^{-1}$. The CV

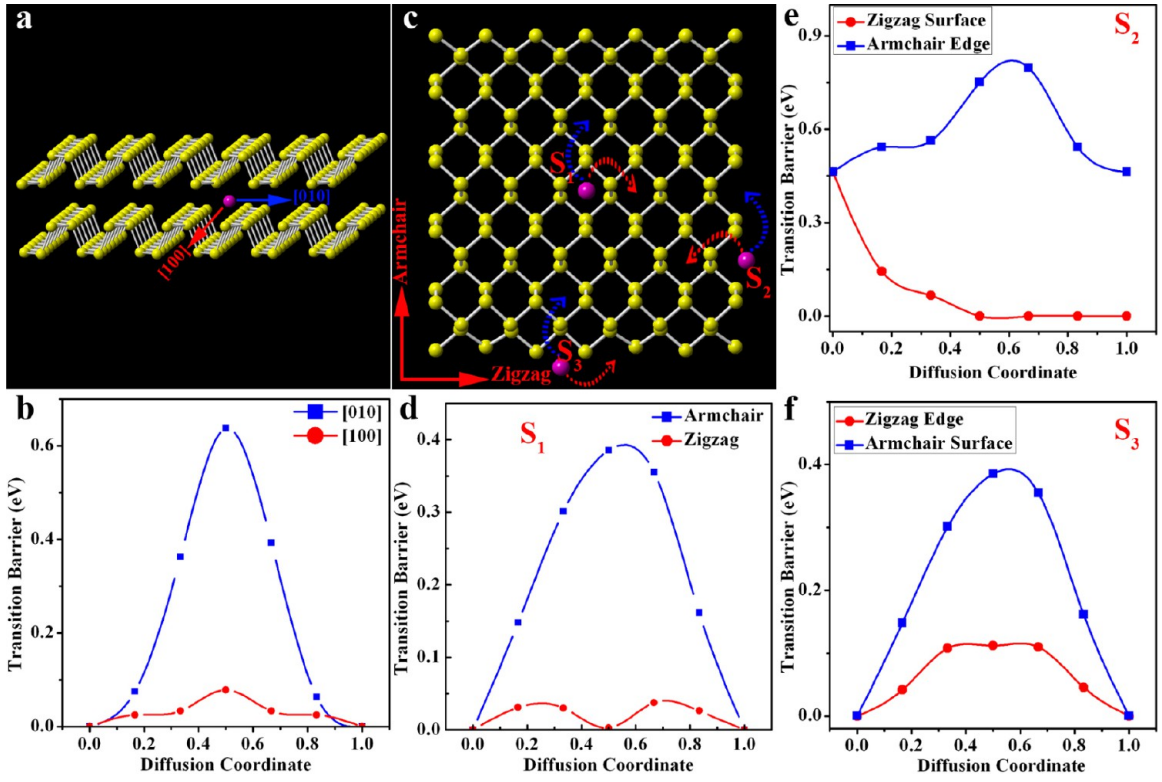


**Figure 5.** DFT simulation of sodium transport in phosphorene. (a) Schematic of sodium ion transport in interlayer of few-layer phosphorene. Phosphorus and sodium atoms are shown in yellow and purple, respectively. (b) Energy profiles for sodium ion diffusion in different directions in few-layer phosphorene. (c) Schematic of sodium ions transport on monolayer phosphorene. $S_1$, $S_2$, and $S_3$ indicate sodium migration on different sites (surface, armchair edge, and zigzag edge, respectively). (d) Energy profiles for sodium diffusion alone the armchair and zigzag surface. (e) Energy profiles for sodium diffusion alone the armchair edge and zigzag surface. (f) Energy profiles for sodium diffusion alone the zigzag edge and armchair surface.



DOI: 10.1021/acs.nanolett.5b04514
*Nano Lett.* 2016, 16, 2240−2247

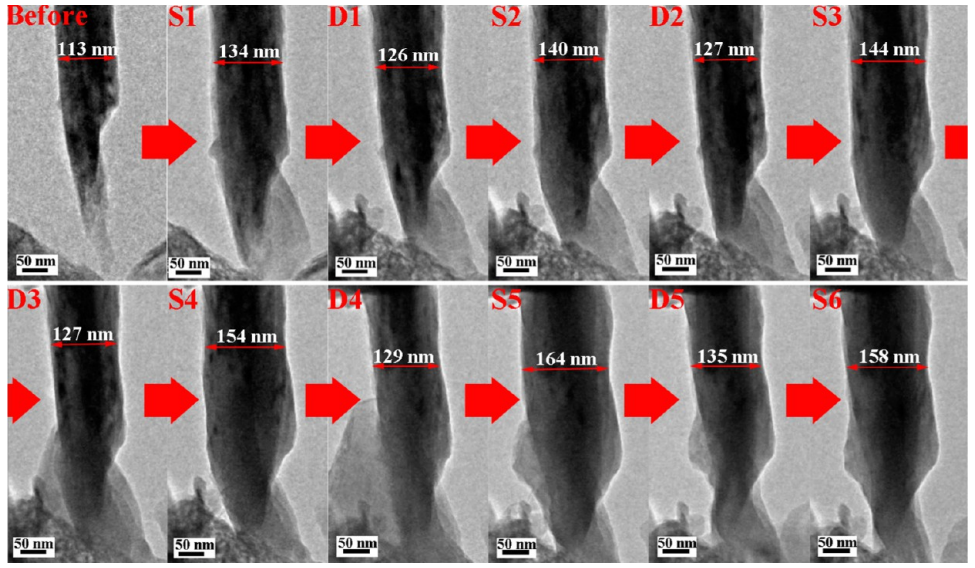


**Figure 6.** In situ TEM investigation of the sodiation/desodiation process of a few-layer phosphorene sample. Here, S and D indicate sodiation and desodiation, respectively. The observation is taken from a side view. We can clearly see the volume change of the sample during cycling.

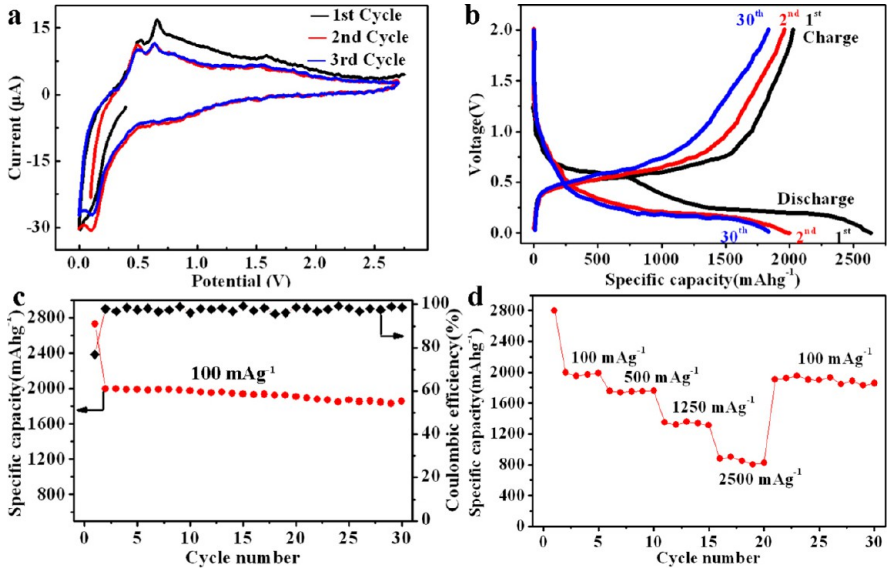


**Figure 7.** Electrochemical performance of phosphorene in half-cells sodium-ion batteries. (a) Cyclic voltammograms of the first three cycles for the phosphorene electrode at a scanning rate of 0.05 mV $S^{-1}$. (b) Galvanostatic discharge/charge curves of the phosphorene electrode. (c) Cycling performance of the phosphorene electrode at a current rate of 100 mA $g^{-1}$. (d) Rate capacity of the phosphorene electrode at different current rate.

peaks are clearly observed near 0.80 and 0.11 V in the cathodic scans corresponding to the sodiation process of the phosphorene electrode. During anodic scans, the peaks near 0.49, 0.65, and 1.51 V are related to the desodiation process of the electrode. Figure 7b shows the charge−discharge behavior of the phosphorene sample at the rate of 100 mA $g^{-1}$. The first cycle shows an extremely high discharge/charge capacity of 2631/2025 mA h $g^{-1}$ with a Coulombic efficiency of 77%. The discharge/charge capacity of the second cycle reduces to 1998/1959 mA h $g^{-1}$ with a really high Coulombic efficiency of 98%. The formation of solid-electrolyte interphase on the phosphorene may be the reason for this capacity loss. The 30th cycle can still retain a high discharge/charge capacity of 1845/1820 mA h $g^{-1}$. As shown in Figure 7c, there is no obvious fading for the capacity of the phosphorene after 30 cycles at 100 mA $g^{-1}$, indicating a stable cycling performance. Figure 6b exhibits the rate cycling behavior of the phosphorene electrode, which displays a reversible capacity of 1970, 1750, 1340, and 850 mA h $g^{-1}$, at 0.04, 0.2, 0.5, and 1 C rates (1C = 2500 $mAg^{-1}$), respectively. Noticeably, significant reversible capacity of 850 mA h $g^{-1}$ was delivered even at the rate of 2500 mA $g^{-1}$, and then the capacity was recovered to 1850 mA h $g^{-1}$.

In summary, we have performed in situ TEM and complementary DFT simulations to reveal the migration pathways for sodium ions inside mono and few-layer phosphorene. It has been found that the early stage of sodiation is associated with the transport of sodium ions along the [100] direction originating from the highly anisotropic diffusion property of sodium ions in both mono and few-layer phosphorene resulting from their puckered structures. Additionally, the zigzag edge of the phosphorene provides a faster diffusion path for the sodium ion in comparison to the armchair



DOI: 10.1021/acs.nanolett.5b04514
Nano Lett. 2016, 16, 2240−2247

edge and surface. We have also investigated the electrochemical performance of the phosphorene electrode in half-cell sodium-ion batteries. The phosphorene sample displays an extremely high capacity, great cycling stability, and good rate capability. Our experimental and theoretical findings provide a profound understanding of ionic transport properties of phosphorene. This knowledge should also provide guidance for optimal electrode design for sodium-ion batteries. Since the sodium ion prefer to diffusion along the [100] direction, minimizing the dimension on the [010] direction of the phosphorene would provide easy diffusion channels, thereby improving the rate capability of the phosphorene nanoribbons for sodium-ion batteries.

**Methods.** *Sample Preparation.* 0.5 mg of BP (purchased from Smart Elements) was ground by a mortar and pestle and then immersed in 10 mL of dimethylformamide (DMF) solvent. The sample was sonicated in a Sonics Vibra-Cell sonicator (130 W) for 15 h and then centrifuged for 30 min at 2000 rpm. The supernatant (the top 80% of the solution) was collected and filtered on a polytetrafluoroethylene (PTFE) filter membrane of 0.1 $\mu$m pore size using a Sigma–Aldrich vacuum filtration setup. The resulting film was then thoroughly washed with a pint of ethanol, water, and isopropyl alcohol (IPA) in sequential order to remove the remaining solvent residue. The film was then immersed in IPA and sonicated to redisperse the flakes in solution. The measured Raman spectrum for the exfoliated phosphorene nanoflakes is shown in Figure S9. The exfoliated phosphorene sample for half-cell sodium ion battery testing was prepared by a similar way but with a large scale (10 mg BP in 100 mL of DMF solvent) and multiple times (20).

*In Situ Experiments.* The schematic of the experimental setups is shown in Figure 2. The phosphorene sample was stick to a gold wire to build an in situ Na-ion cell inside the TEM. The gold wire also acted as a current collector on the nanoflakes side. Sodium metal that served as the counter electrode was scratched by a tungsten wire inside the glovebox filled with Ar. The two electrodes were mounted onto a Nanofactory Instruments scanning tunneling microscope (STM)-TEM in situ sample holder, which was transferred in an airtight container and loaded into the TEM column. The naturally grown $Na_2O$ and NaOH layer on the surface of the sodium metal served as the solid electrolyte for Na transport. The ($Na_2O$ + NaOH)/Na electrode side was moved forward to contact one of phosphorene nanoflakes. Once a reliable electrical contact was built, potentials of −0.5 V were applied to the phosphorene flake to initiate the sodiation. The in situ desodiation was realized by applying a positive bias of 2 V. The in situ sodiation/desodiation experiments were carried out inside an aberration-corrected JEOL JEM-ARM200CF STEM operated at 80 KV. The HAADF images were acquired using a 22-mrad-probe convergence semiangle and a 90 mrad inner-detector angle at 200 kV. The in situ lithiation experiment was conducted in a similar way with the exception that $Li_2O$/Li electrode was used as the counter electrode.

*DFT Simulation.* All calculations were conducted using the Quantum-ESPRESSO package[47] in density functional theory framework. We employed ultrasoft pseudopotentials[48] as well as the generalized gradient approximation in the Perdew–Burke–Ernzerhof parametrization[49] of the exchange correlation functional. A self-consistency energy accuracy of $1.4 \times 10^{-9}$ eV, residual forces below $2.6 \times 10^{-3}$ eV/Å, and a total energy convergence of $1.4 \times 10^{-4}$ eV were achieved. A 4 × 5 supercell was used to model phosphorene and a 15 Å thick vacuum layer was adopted to prevent self-interaction by the periodic boundary conditions and the lattice constant of phosphorene. To evaluate the mobility of Na, we first calculate the most stable position for single Na on phosphorene. We calculated the transition barriers between neighboring stable sites by nudged elastic band calculations.[50−52]

*Electrochemical Testing.* The electrode slurry contains 70 wt % of electrode material (BP and exfoliated phosphorene), 15 wt % super P carbon and 15 wt % of sodium carboxmethylcellulose (NaCMC) binder in *N*-methylpyrrolidinone (NMP). The mixture was homogeneously mixed by ball-milling for 1.5 h, tape casted onto a 150 $\mu$m thick Cu foil, and dried at 75 °C for 4 h, and followed by being thoroughly dried at 75 °C overnight under vacuum. The composite electrode loading was 1.4 mg $cm^{-2}$ and approximately 0.98 mg $cm^{-2}$ as the phosphorene active materials. Electrochemical measurement was carried out using the 2025 coin cells with Na metal as the counter electrode, a 25 $\mu$m thick polypropylene separator, and 1 M $NaClO_4$ in propylene carbonate with addition of 5 vov % fluoroethylene carbonate (FEC) as the electrolyte. The cells were cycled between 0 to 2.0 V, and the cyclic voltammograms were scanned from 0 to 2.75 V at a rate of 0.05 mV $s^{-1}$.

## ■ ASSOCIATED CONTENT

### Supporting Information

The Supporting Information is available free of charge on the ACS Publications website at DOI: 10.1021/acs.nanolett.5b04514.

Additional figures and experimental details (PDF)
Movie S1 (AVI)
Movie S2 (AVI)
Movie S3 (AVI)
Movie S4 (AVI)

## ■ AUTHOR INFORMATION


### Corresponding Authors

*E-mail: rsyassar@uic.edu.
*E-mail: mashayek@uic.edu.


### Author Contributions

A.N. and Y.C.C. contributed equally. A.N. carried out the TEM experiments and made the data analysis under the direction of R.S.Y. and F.M. R.S.Y. initiated the project and created the experimental protocols. Y.C.C. and F.M. performed DFT calculations. S.N. performed the (S)TEM images simulations. W.L. conducted the Raman testing of the sample. T.F. P.Y. and A.S.K. supplied the phosphorene samples. Y.F.Y. and L.C. did the half-cell sodium-ion batteries electrochemical performance testing. B.S. did the design of schematic of experimental setups. A.N. and R.S.Y. wrote the manuscript, and all the authors contributed to the discussion and revision of the manuscript.

### Notes

The authors declare no competing financial interest.

## ■ ACKNOWLEDGMENTS


R. Shahbazian-Yassar acknowledges the financial support from the National Science Foundation (Award No. CMMI-1619743). Y. Cheng was supported by the National Natural Science Foundation of China (11504169 and 61575094). The acquisition of the UIC JEOL JEM-ARM200CF is supported by an MRI-R2 grant from the National Science Foundation (Award No. DMR-0959470). Helpful discussion from Dr. Robert F. Klie is acknowledged. We also thank UIC Research




DOI: 10.1021/acs.nanolett.5b04514
*Nano Lett.* 2016, 16, 2240−2247

Resources Center for assisting the usage of their equipment and instrumentation.

## REFERENCES


(1) Maier, J. *Nat. Mater.* **2005**, *4*, 805−815.
(2) Yoo, E.; Kim, J.; Hosono, E.; Zhou, H.-s.; Kudo, T.; Honma, I. *Nano Lett.* **2008**, *8*, 2277−2282.
(3) Pollak, E.; Geng, B.; Jeon, K.-J.; Lucas, I. T.; Richardson, T. J.; Wang, F.; Kostecki, R. *Nano Lett.* **2010**, *10*, 3386−3388.
(4) Chang, K.; Chen, W. *ACS Nano* **2011**, *5*, 4720−4728.
(5) Acerce, M.; Voiry, D.; Chhowalla, M. *Nat. Nanotechnol.* **2015**, *10*, 313−318.
(6) Lukatskaya, M. R.; Mashtalir, O.; Ren, C. E.; Dall'Agnese, Y.; Rozier, P.; Taberna, P. L.; Naguib, M.; Simon, P.; Barsoum, M. W.; Gogotsi, Y. *Science* **2013**, *341*, 1502−1505.
(7) Tang, Q.; Zhou, Z.; Shen, P. *J. Am. Chem. Soc.* **2012**, *134*, 16909−16916.
(8) Liu, H.; Neal, A. T.; Zhu, Z.; Luo, Z.; Xu, X.; Tománek, D.; Ye, P. D. *ACS Nano* **2014**, *8*, 4033−4041.
(9) Xia, F.; Wang, H.; Jia, Y. *Nat. Commun.* **2014**, *5*, 4458.
(10) Qiao, J.; Kong, X.; Hu, Z.-X.; Yang, F.; Ji, W. *Nat. Commun.* **2014**, *5*, 4475.
(11) Yuan, H.; Liu, X.; Afshinmanesh, F.; Li, W.; Xu, G.; Sun, J.; Lian, B.; Curto, A. G.; Ye, G.; Hikita, Y. *Nat. Nanotechnol.* **2015**, *10*, 707−713.
(12) Wang, X.; Jones, A. M.; Seyler, K. L.; Tran, V.; Jia, Y.; Zhao, H.; Wang, H.; Yang, L.; Xu, X.; Xia, F. *Nat. Nanotechnol.* **2015**, *10*, 517−521.
(13) Favron, A.; Gaufrès, E.; Fossard, F.; Phaneuf-L'Heureux, A.-L.; Tang, N. Y.; Lévesque, P. L.; Loiseau, A.; Leonelli, R.; Francoeur, S.; Martel, R. *Nat. Mater.* **2015**, *14*, 826−832.
(14) Kim, J.; Baik, S. S.; Ryu, S. H.; Sohn, Y.; Park, S.; Park, B.-G.; Denlinger, J.; Yi, Y.; Choi, H. J.; Kim, K. S. *Science* **2015**, *349*, 723−726.
(15) Guo, G.-C.; Wei, X.-L.; Wang, D.; Luo, Y.; Liu, L.-M. *J. Mater. Chem. A* **2015**, *3*, 11246−11252.
(16) Yao, Q.; Huang, C.; Yuan, Y.; Liu, Y.; Liu, S.; Deng, K.; Kan, E. *J. Phys. Chem. C* **2015**, *119*, 6923−6928.
(17) Kulish, V. V.; Malyi, O. I.; Persson, C.; Wu, P. *Phys. Chem. Chem. Phys.* **2015**, *17*, 13921−13928.
(18) Zhao, S.; Kang, W.; Xue, J. *J. Mater. Chem. A* **2014**, *2*, 19046−19052.
(19) Li, W.; Yang, Y.; Zhang, G.; Zhang, Y.-W. *Nano Lett.* **2015**, *15*, 1691−1697.
(20) Sun, J.; Lee, H.-W.; Pasta, M.; Yuan, H.; Zheng, G.; Sun, Y.; Li, Y.; Cui, Y. *Nat. Nanotechnol.* **2015**, *10*, 980−985.
(21) Buscema, M.; Groenendijk, D. J.; Steele, G. A.; van der Zant, H. S.; Castellanos-Gomez, A. *Nat. Commun.* **2014**, *5*, 4651.
(22) Deng, Y.; Luo, Z.; Conrad, N. J.; Liu, H.; Gong, Y.; Najmaei, S.; Ajayan, P. M.; Lou, J.; Xu, X.; Ye, P. D. *ACS Nano* **2014**, *8*, 8292−8299.
(23) Dai, J.; Zeng, X. C. *J. Phys. Chem. Lett.* **2014**, *5*, 1289−1293.
(24) Koenig, S. P.; Doganov, R. A.; Schmidt, H.; Neto, A. C.; Oezyilmaz, B. *Appl. Phys. Lett.* **2014**, *104*, 103106.
(25) Li, L.; Yu, Y.; Ye, G. J.; Ge, Q.; Ou, X.; Wu, H.; Feng, D.; Chen, X. H.; Zhang, Y. *Nat. Nanotechnol.* **2014**, *9*, 372−377.
(26) Zhang, J.; Liu, H.; Cheng, L.; Wei, J.; Liang, J.; Fan, D.; Shi, J.; Tang, X.; Zhang, Q. *Sci. Rep.* **2014**, *4*, 6452.
(27) Lv, H.; Lu, W.; Shao, D.; Sun, Y. *Phys. Rev. B: Condens. Matter Mater. Phys.* **2014**, *90*, 085433.
(28) Fei, R.; Faghaninia, A.; Soklaski, R.; Yan, J.-A.; Lo, C.; Yang, L. *Nano Lett.* **2014**, *14*, 6393−6399.
(29) Yasaei, P.; Behranginia, A.; Foroozan, T.; Asadi, M.; Kim, K.; Khalili-Araghi, F.; Salehi-Khojin, A. *ACS Nano* **2015**, *9*, 9898−9905.
(30) Morita, A. *Appl. Phys. A: Solids Surf.* **1986**, *39*, 227−242.
(31) Jamieson, J. C. *Science* **1963**, *139*, 1291−1292.
(32) Yasaei, P.; Kumar, B.; Foroozan, T.; Wang, C.; Asadi, M.; Tuschel, D.; Indacochea, J. E.; Klie, R. F.; Salehi-Khojin, A. *Adv. Mater.* **2015**, *27*, 1887−1892.
(33) Etacheri, V.; Marom, R.; Elazari, R.; Salitra, G.; Aurbach, D. *Energy Environ. Sci.* **2011**, *4*, 3243−3262.
(34) Tarascon, J.-M.; Armand, M. *Nature* **2001**, *414*, 359−367.
(35) Palomares, V.; Serras, P.; Villaluenga, I.; Hueso, K. B.; Carretero-González, J.; Rojo, T. *Energy Environ. Sci.* **2012**, *5*, 5884−5901.
(36) Yabuuchi, N.; Kubota, K.; Dahbi, M.; Komaba, S. *Chem. Rev.* **2014**, *114*, 11636−11682.
(37) Pan, H.; Hu, Y.-S.; Chen, L. *Energy Environ. Sci.* **2013**, *6*, 2338−2360.
(38) Slater, M. D.; Kim, D.; Lee, E.; Johnson, C. S. *Adv. Funct. Mater.* **2013**, *23*, 947−958.
(39) Kim, S. W.; Seo, D. H.; Ma, X.; Ceder, G.; Kang, K. *Adv. Energy Mater.* **2012**, *2*, 710−721.
(40) Jing, Y.; Zhou, Z.; Cabrera, C. R.; Chen, Z. *J. Phys. Chem. C* **2013**, *117*, 25409−25413.
(41) Uthaisar, C.; Barone, V. *Nano Lett.* **2010**, *10*, 2838−2842.
(42) Ling, C.; Mizuno, F. *Phys. Chem. Chem. Phys.* **2014**, *16*, 10419−10424.
(43) Kulish, V. V.; Malyi, O. I.; Ng, M.-F.; Chen, Z.; Manzhos, S.; Wu, P. *Phys. Chem. Chem. Phys.* **2014**, *16*, 4260−4267.
(44) Mortazavi, M.; Wang, C.; Deng, J.; Shenoy, V. B.; Medhekar, N. V. *J. Power Sources* **2014**, *268*, 279−286.
(45) Castellanos-Gomez, A.; Vicarelli, L.; Prada, E.; Island, J. O.; Narasimha-Acharya, K.; Blanter, S. I.; Groenendijk, D. J.; Buscema, M.; Steele, G. A.; Alvarez, J. *2D Mater.* **2014**, *1*, 025001.
(46) Hembram, K.; Jung, H.; Yeo, B. C.; Pai, S. J.; Kim, S.; Lee, K.-R.; Han, S. S. *J. Phys. Chem. C* **2015**, *119*, 15041−15046.
(47) Giannozzi, P.; Baroni, S.; Bonini, N.; Calandra, M.; Car, R.; Cavazzoni, C.; Ceresoli, D.; Chiarotti, G. L.; Cococcioni, M.; Dabo, I. *J. Phys.: Condens. Matter* **2009**, *21*, 395502.
(48) Vanderbilt, D. *Phys. Rev. B: Condens. Matter Mater. Phys.* **1990**, *41*, 7892.
(49) Perdew, J. P.; Burke, K.; Ernzerhof, M. *Phys. Rev. Lett.* **1996**, *77*, 3865.
(50) E, W.; Ren, W.; Vanden-Eijnden, E. *Phys. Rev. B: Condens. Matter Mater. Phys.* **2002**, *66*, 052301.
(51) Henkelman, G.; Jónsson, H. *J. Chem. Phys.* **1999**, *111*, 7010−7022.
(52) Caspersen, K. J.; Carter, E. A. *Proc. Natl. Acad. Sci. U. S. A.* **2005**, *102*, 6738−6743.




DOI: 10.1021/acs.nanolett.5b04514
*Nano Lett.* 2016, 16, 2240−2247